Electronic processes in fast thermite chemical reactions: A first-principles molecular dynamics study

Fuyuki Shimojo,[1,2] Aiichiro Nakano,[1] Rajiv K. Kalia,[1] and Priya Vashishta[1]
[1]*Collaboratory for Advanced Computing and Simulations, Department of Computer Science, Department of Physics and Astronomy, Department of Chemical Engineering and Materials Science, University of Southern California, Los Angeles, California 90089-0242, USA*
[2]*Department of Physics, Kumamoto University, Kumamoto 860-8555, Japan*
(Received 28 August 2007; revised manuscript received 7 January 2008; published 5 June 2008)

Rapid reaction of a molten metal with an oxide is the key to understanding recently discovered fast reactions in nanothermite composites. We have investigated the thermite reaction of Fe_2O_3 with aluminum by molecular dynamics simulations with interatomic forces calculated quantum mechanically in the framework of the density functional theory. A redox reaction to form iron metal and Al_2O_3 initiates with the rapid formation of Al-O bonds at the interface within 1 ps, followed by the propagation of the combustion front with a velocity of 70 m/s for at least 5 ps at 2000 K. The reaction time for an oxygen atom to change character from Fe_2O_3 type to Al_2O_3 type at the interface is estimated to be 1.7 ± 0.9 ps, and bond-overlap population analysis has been used to calculate reaction rates.

DOI: 10.1103/PhysRevE.77.066103 PACS number(s): 82.20.Db, 02.70.Ns, 61.46.−w, 71.15.Pd

I. INTRODUCTION

Highly exothermic reaction between a metal and an oxide, commonly known as thermite reaction, is widely utilized in the synthesis and processing of materials [1]. In addition to metallurgical applications, thermite reactions are used for the synthesis of ceramics and composites that have chemical stability and high melting temperatures. Due to the enormous energy release associated with the formation of a more stable oxide by the reduction-oxidation (redox) reaction, these reactions also have promising energetic material applications [2–7]. To achieve high reaction rates through increased contact areas between fuel metals and reactant oxides, nanostructured composite materials have been developed. Recent experimental studies on the combustion properties of nanothermites, such as $Al+Fe_2O_3$ [8] and $Al+MoO_3$ [9], have shown that flame propagation speeds reach several hundred m/s when the size of Al nanoparticles is reduced to less than 100 nm, in contrast to cm/s for traditional thermites.

The fast reaction of the nanothermites cannot be explained by a conventional mechanism based on the diffusion of Al and O atoms in oxides. Instead it has been suggested that the fast flame propagation is due to spallation of the oxide shell covering the melted Al nanoparticles [10]. Since a consensus on the dominant atomistic mechanism for the fast nanothermite reaction has not been reached yet, it is crucial to understand how the reaction of molten metal with an oxide is initiated in picoseconds. (Note that a 400 m/s combustion front propagates through a typical 4 nm oxide shell in 10 ps.)

Mechanical properties of nanocrystalline α-Fe_2O_3 +fcc-Al composites at room temperature have been studied by molecular dynamics (MD) simulations with a reactive empirical potential model [11,12]. It is found that the deformation of nanocomposites under uniaxial strain is strongly affected by the Al-Fe_2O_3 interfaces which are determined by volume fractions and grain sizes. However, MD simulation of the initiation of thermite reaction is yet to be performed at the level of quantum-mechanical (QM) accuracy. This paper reports the results of MD simulations with interatomic forces computed quantum mechanically in the framework of the density functional theory (DFT) to study initial atomistic processes during the thermite reaction between Al metal and hematite Fe_2O_3.

II. METHOD OF CALCULATION

Our electronic structure calculation in the DFT framework uses a generalized gradient approximation [13] for the exchange-correlation energy. The electronic wave functions and the electron density are expanded in plane-wave basis sets with cutoff energies of 30 and 200 Ry, respectively. The energy functional is minimized iteratively using a preconditioned conjugate-gradient method [14,15]. Ultrasoft pseudopotentials [16] are used to describe the interaction between valence electrons and ions. The simulation involves 192 (24 Fe_2O_3+72 Al) atoms in an orthorhombic supercell with dimensions of $(L_x, L_y, L_z) = (10.1\ \text{Å}, 8.7\ \text{Å}, 28.2\ \text{Å})$ with periodic boundary conditions. The initial configuration of atoms is shown in Fig. 1. The hematite (Fe_2O_3) crystal is cut along the (0001) planes so as to expose Fe planes, and is placed in the supercell with the (0001) direction parallel to the z direction (Fig. 1). The Fe planes of the hematite are attached to the (111) planes of the Al fcc crystal at the two interfaces. Note that the atomic geometries of the two interfaces are different from each other as shown in Fig. 1. The MD simulations are carried out at a temperature of 2000 K in the canonical ensemble using the Nosè-Hoover thermostat technique [17]. The equations of motion are solved numerically using an explicit reversible integrator [18] with a time step of 35 a.u. (~0.84 fs).

III. RESULTS AND DISCUSSIONS

A. Time evolution of atomic structures

The time evolution of atomic configuration is shown in Fig. 2, where the side (yz) views of atomic configuration are

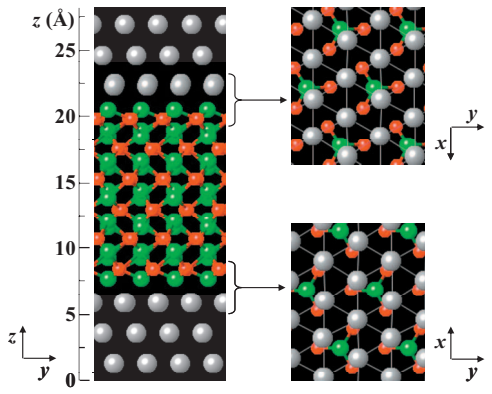

FIG. 1. (Color) Initial configuration of atoms. The green, red, and gray spheres show the positions of Fe, O, and Al atoms, respectively. The left panel shows the side (yz) view of the entire system, while the right panel shows the top (xy) views of the two Al/Fe_2O_3 interfaces. The x direction corresponds to the $\langle 110\rangle$ direction of the fcc Al and the $\langle 2\bar{1}\bar{1}0\rangle$ direction of the hematite Fe_2O_3. In the left panel, a scale marked in Å is given in the z direction.

displayed at time intervals of about 1.7 ps (7×10^4 a.u.). It is demonstrated that the oxygen atoms in hematite migrate into the aluminum metal to form aluminum oxide and leaves behind liquid iron, which means that our simulation successfully reproduces the thermite reaction in the Fe_2O_3/Al system consisting initially of thin hematite and aluminum layers. Although the reaction occurs at both of the upper and lower interfaces, the atomic arrangements in the early stages of the reaction are rather different at the two interfaces. As shown in the snapshots at 1.7 and 3.4 ps, some Fe and O atoms migrate across the upper interface into the aluminum side, whereas the boundary between iron oxide and aluminum oxide is clearly seen at the lower interface. Note that two Fe atoms are located always at the upper oxidation front and are separated from iron metal by aluminum oxide (see the upper part of the snapshots). The difference in the reaction at the upper and lower Fe_2O_3/Al interfaces arises from the different initial atomic geometries of the two interfaces: Al atoms reside on top of Fe atoms at the upper interface, while Al atoms reside on top of O atoms at the lower interface (see Fig. 1).

To see the initial change of interface structures more clearly, we show the time evolution of atomic configuration

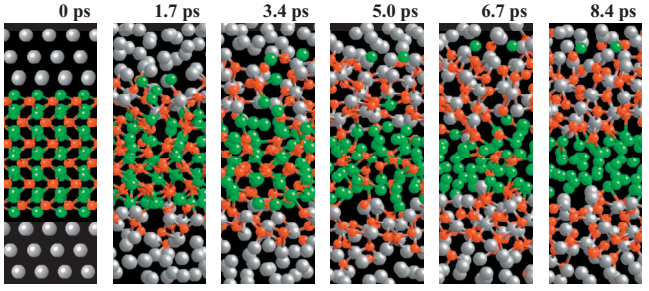

FIG. 2. (Color) Time evolution of the side (yz) view of atomic configuration at time intervals of about 1.7 ps (7×10^4 a.u.). The green, red, and gray spheres are the Fe, O, and Al atoms, respectively.

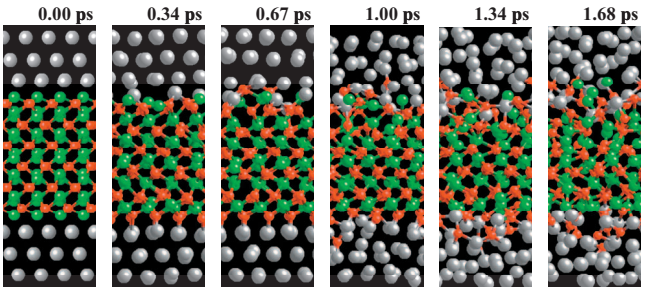

FIG. 3. (Color) Time evolution of the side (yz) view of atomic configuration at time intervals of about 0.34 ps (1.4×10^4 a.u.). The green, red, and gray spheres are the Fe, O, and Al atoms, respectively.

at time intervals of about 0.34 ps (1.4×10^4 a.u.) in Fig. 3. It is seen that, at the lower interface, each oxygen atom migrates directly to the nearest Al atom to form an Al-O bond when the reaction starts, which prevents Fe atoms from diffusing into the aluminum side. On the other hand, Al-O bonds are formed nonuniformly at the upper interface from the beginning of the reaction, and the atomic geometry becomes more disordered compared with the lower interface. We observe that some Al atoms migrate into the iron oxide side to form Al-O bonds, and the two Fe atoms are forced into the aluminum side by the intense reaction inside iron oxide.

Figure 4 shows the time evolution of the partial number densities $\rho_\alpha(z)$ of α-type atom as a function of the z coordinate. In the figure, the green dotted, red solid, and black dashed lines are $\rho_{Fe}(z)$, $\rho_O(z)$, and $\rho_{Al}(z)$, respectively, which were averaged over about 0.3 ps at each time. At 0 ps, there are sharp peaks in the profiles of all $\rho_\alpha(z)$ reflecting the initial crystalline configuration. In the distribution of oxygen atoms, six layers exist in the initial hematite crystal, as $\rho_O(z)$ has six peaks at 0 ps. Hereafter, we call them the first, second, …, and sixth oxygen layers from bottom to top as shown in the figure at 0 ps. The peaks of $\rho_O(z)$ partially remain up to about 3 ps, and its profile becomes broad over 4 ps. It is found that the peak of $\rho_O(z)$ corresponding to the first oxygen layer at about $z=8$ Å exchanges its position with the peak of $\rho_{Al}(z)$ at $z\sim6$ Å in the time interval between 1 and 2 ps, while their neighbor peaks of $\rho_O(z)$ for the second oxygen layer at $z\sim11$ Å and of $\rho_{Fe}(z)$ at $z\sim9$ Å are almost unchanged up to 2 ps. This means that only the first layer of oxygen atoms reacts mainly with aluminum metal in the early stage of the reaction at the lower interface. On the other hand, at the upper interface, there is no clear exchange between the layers of O and Al, and oxygen atoms in the fifth layer at $z\sim17$ Å as well as those in the sixth layer at $z\sim19$ Å react with aluminum before 2 ps. At 3 ps, while the peak of the second oxygen layer at $z\sim11$ Å still exists at the lower interface, no corresponding peak of the fifth oxygen layer, which is the second counting from the upper interface, is present. Above 4 ps, oxygen atoms diffuse into both aluminum sides to form aluminum oxide, and Fe atoms aggregate into pure iron in the liquid state.

B. Combustion front propagation

The positions $z_c(t)$ of the combustion fronts are calculated from the coordinates of oxygen atoms at the forefronts of

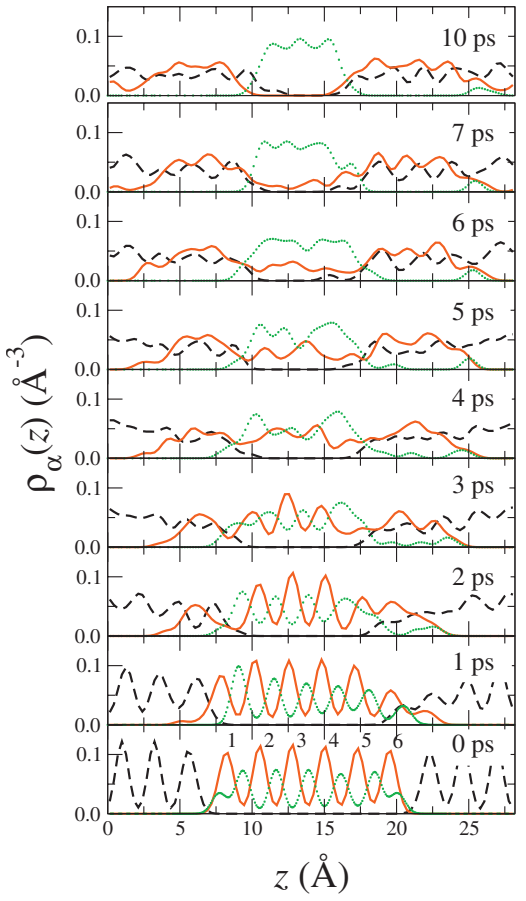

FIG. 4. (Color) Time evolution of the partial number densities $\rho_\alpha(z)$ of α-type atoms for α=Fe (green dotted lines), O (red solid lines), and Al (black dashed lines).

oxidation at the upper and lower interfaces. We take the average $\langle z(t)\rangle$ of z coordinates of six oxygen atoms on each oxidation front, and define $z_c(t)$ as $z_c(t)=|\langle z(t)\rangle-\langle z(0)\rangle|$. Figure 5 shows the time evolution of $z_c(t)$. For $t<1$ ps, $z_c(t)$ increase rapidly as oxygen atoms migrate to approach Al atoms within Fe_2O_3. After the first layer of Al-O bonds is formed within 1 ps, the oxidation fronts at the both interfaces propagate linearly in time. From the slope of $z_c(t)$ for $1<t<6$ ps, the velocity of the combustion front is estimated to

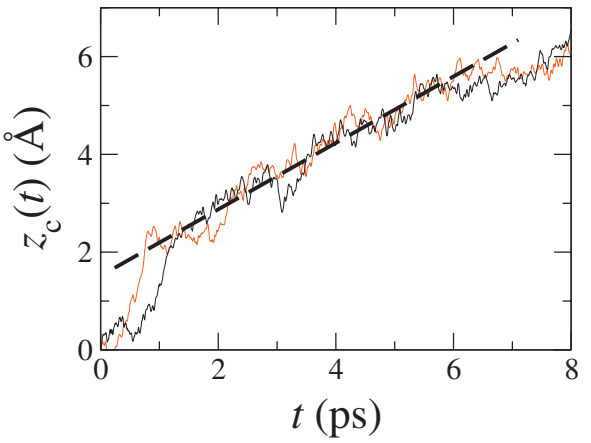

FIG. 5. (Color) Time evolution of the positions $z_c(t)$ of the upper (black) and lower (red) combustion fronts.

be ~70 m/s. For $t>6$ ps, $z_c(t)$ deviates from the linearity due to the near completion of the reaction.

C. Population analysis

To quantify the change in the bonding properties of atoms associated with the redox reaction, we use a population analysis [19] by expanding the electronic wave functions in an atomic-orbital basis set [20,21]. The population analysis is a useful tool to investigate the bonding nature of high-temperature materials, since it describes intuitively the electronic structure of not only molecules but also disordered condensed systems in terms of chemical concepts [20]. Here, we formulate the population analysis based on the plane-wave (PW) basis set with the ultrasoft pseudopotentials [22]. Note that a generalization of the formulation to the projector-augmented-wave method [23], which is an all-electron electronic-calculation method within the frozen-core approximation, is straightforward.

To project the self-consistent wave functions $\psi_n(\boldsymbol{r})$ obtained with the PW basis into the subspace generated by the atomic basis $\{\phi_\mu\}$, the projection operator $\hat{P}$ is defined as [20–22]

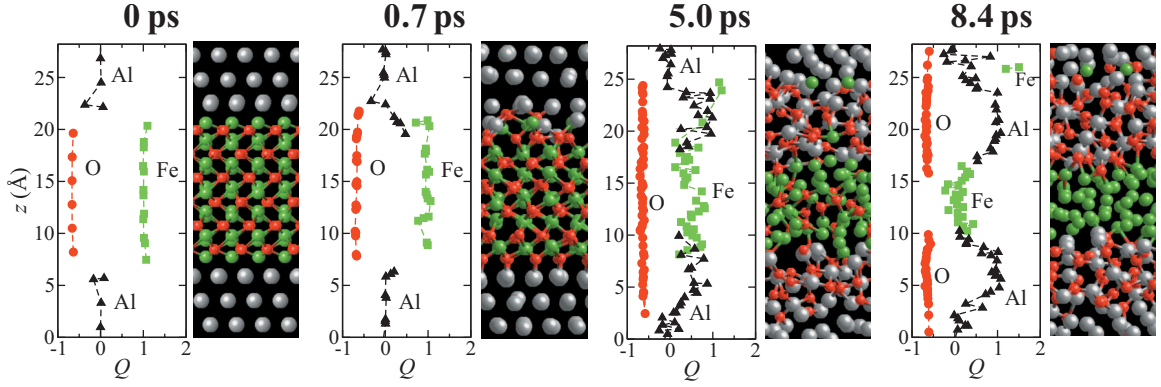

FIG. 6. (Color) Time evolution of the Mulliken charges $Q_\alpha(z)$ for Fe (green squares), O (red circles), and Al (black triangles) as a function of the z position. In the atomic configurations, the green, red and gray spheres are the Fe, O, and Al atoms, respectively.

$$\hat{P} = \sum_{\mu,\nu} |\phi_\mu\rangle S^{-1}_{\mu\nu} \langle \phi_\nu | \hat{s}, \tag{1}$$

where

$$S_{\mu v} = \langle \phi_\mu | \hat{s} | \phi_\nu \rangle \quad \text{and} \quad \hat{s} = 1 + \sum_{\mu\nu} q_{\mu\nu} |\beta_\mu\rangle \langle \beta_\nu| \tag{2}$$

with $\beta_\mu(\boldsymbol{r})$ and $q_{\mu\nu}$ being the localized functions and the augmentation charges, respectively, in the ultrasoft pseudopotentials [16]. Note that the formulation for the norm-conserving pseudopotentials is obtained if $\hat{s}=1$. The projected wave functions $\chi_n(\boldsymbol{r})$ are obtained by operating $\hat{P}$ on $\psi_n(\boldsymbol{r})$ as

$$|\chi_n\rangle = \hat{P}|\psi_n\rangle = \sum_\mu |\phi_\mu\rangle C_{\mu n} \tag{3}$$

with

$$C_{\mu n} = \sum_\nu S^{-1}_{\mu\nu} \langle \phi_\nu | \hat{s} | \psi_n \rangle. \tag{4}$$

Generally $\chi_n(\boldsymbol{r})$ are not orthonormalized; $R_{nm}=\langle \chi_n|\hat{s}|\chi_m\rangle \neq \delta_{nm}$. To ensure the charge conservation, the dual of $\chi_n(\boldsymbol{r})$ is introduced as [20]

$$|\chi^n\rangle = \sum_m |\chi_m\rangle R^{-1}_{mn} = \sum_\mu |\phi_\mu\rangle C^{\mu n} \tag{5}$$

with

$$C^{\mu n} = \sum_m C_{\mu m} R^{-1}_{mn} \tag{6}$$

so that $\langle \chi^n | \hat{s} | \chi_m \rangle = \delta_{nm}$.

With respect to the nth electronic state, the partial gross atomic population $N^{(n)}_\mu$ associated with the μth atomic basis function and the partial bond-overlap population $O^{(n)}_{\mu\nu}$ associated with the μth and νth atomic basis functions are defined as [19]

$$N^{(n)}_\mu = \sum_\nu C^{\nu n} S_{\nu\mu} C_{\mu n} \tag{7}$$

and

$$O^{(n)}_{\mu\nu} = \frac{1}{2}(C^{\mu n} S_{\mu\nu} C_{\nu n} + C^{\nu n} S_{\nu\mu} C_{\mu n}), \tag{8}$$

respectively. The gross atomic population N_i on ith atom and the bond-overlap population O_{ij} for a pair of ith and jth atoms are obtained by summing $N^{(n)}_\mu$ and $O^{(n)}_{\mu\nu}$, respectively, as follows:

$$N_i = \sum_n \sum_{\mu\in i} f_n N^{(n)}_\mu \tag{9}$$

and

$$O_{ij} = \sum_n \sum_{\mu\in i} \sum_{\nu\in j} f_n O^{(n)}_{\mu\nu}, \tag{10}$$

where f_n is the electronic occupation number of the nth electronic state. To measure the atomic charge associated with each atom, it is beneficial to define the gross charge (hereafter called Mulliken charge) Q_i as [19] $Q_i=N^0_i-N_i$, where N^0_i is the total number of valence electrons in the ground state of the free neutral atom.

Here, we calculate the Mulliken charge $Q_i(t)$ and the bond-overlap population $O_{ij}(t)$ as a function of time t. It should be noted that a different set of atomic-orbital bases would give different values of $Q_i(t)$ and $O_{ij}(t)$ in a strict sense, since the atomic-orbital basis used in the expansion of the wave functions is not unique. Therefore, we need to be cautious in choosing the basis, and it is desirable to reduce the charge spillage [20], which estimates the error in the expansion, as much as possible to avoid such ambiguity. A natural choice is to use the eigenfunctions of the atomic pseudopotentials used in the simulation. We obtain numerical eigenfunctions for a chosen atomic energy so that the first node occurs at the desired cutoff radius (5 Å) [24], and use them as the basis orbitals. To increase the efficiency of the expansion, the numerical basis orbitals are augmented by the split-valence method [25]. The resulting charge spillage is only 0.2%, indicating that our basis orbitals are of high quality.

D. Mulliken charges

Figure 6 shows the time evolution of the Mulliken charges $Q_\alpha(z)$ as a function of the z coordinate for α=Fe (green squares), O (red circles), and Al (black triangles). The atomic configuration corresponding to each time is also displayed in the figure. At 0 ps, $Q_{\mathrm{O}}(z)$ and $Q_{\mathrm{Fe}}(z)$ depend weakly on the z coordinate even at the two interfaces as well as on the inside of the hematite crystal. The values of $Q_{\mathrm{Al}}(z)$ are nearly zero in the aluminum metal, and have some deviations from zero at the interfaces. At 0.7 ps, $Q_{\mathrm{Al}}(z)$ increases at the upper interface due to the reaction, while $Q_\alpha(z)$ are almost unchanged at the lower interface. At 5.0 ps, the reaction progresses at both interfaces, and $Q_\alpha(z)$ for Al and Fe fluctuate greatly depending on surrounding atomic configurations. It should be emphasized that the charges of oxygen $Q_{\mathrm{O}}(z)$ are nearly constant during the thermite reaction. At 8.4 ps, pure liquid iron and aluminum oxide are formed, and the values of $Q_{\mathrm{Fe}}(z)$ and $Q_{\mathrm{Al}}(z)$ are nearly zero and one, respectively, except for the interfaces. It is seen that there are two Fe atoms at the reaction front at $z\sim 26$ Å, and they have high values of $Q_{\mathrm{Fe}}(z)$.

E. Bond-overlap population

Using the bond-overlap populations $O_{ij}(t)$ for atomic pairs, we define the sum of the bond-overlap population (SBOP) for each oxygen atom. The partial SBOP $O^\alpha_i(t)$ for the ith oxygen atom is defined as

$$O^\alpha_i(t) = \sum_{j\in\alpha} O_{ij}(t), \tag{11}$$

where α is Fe or Al. The total SBOP is calculated as $O_i(t) = O^{\mathrm{Fe}}_i(t) + O^{\mathrm{Al}}_i(t)$. Figure 7 shows the time evolution of $O_i(t)$ and $O^\alpha_i(t)$ associated with one of the oxygen atoms. The atomic configurations around the oxygen atom at different times are also shown in Fig. 7. For $t<0.2$ ps, the oxygen

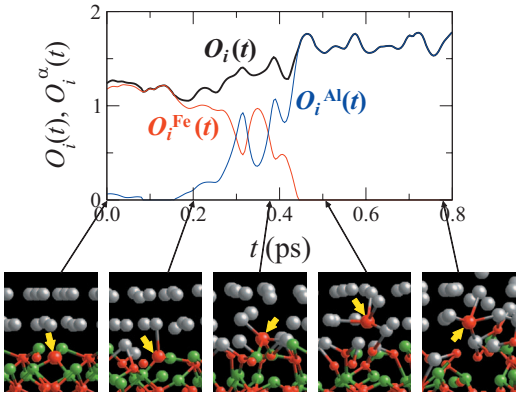

FIG. 7. (Color) (top panel) Time evolution of the total and partial SBOP, $O_i(t)$ and $O_i^{\alpha}(t)$, associated with an oxygen atom. The black, red, and blue curves show $O_i(t)$, $O_i^{\mathrm{Fe}}(t)$, and $O_i^{\mathrm{Al}}(t)$, respectively. (Bottom panel) Atomic configurations near the oxygen atom of interest (pointed by yellow arrows) at different times. The green, red, and gray spheres are Fe, O, and Al atoms, respectively.

atom resides in the iron oxide region, and $O_i^{\mathrm{Fe}}(t)$ has finite values while $O_i^{\mathrm{Al}}(t)$ is nearly zero. At $t \sim 0.2$ ps, the oxygen atom starts to migrate into the aluminum side and $O_i^{\mathrm{Al}}(t)$ begins to increase. For 0.3 ps $< t <$ 0.4 ps, $O_i^{\mathrm{Fe}}(t)$ and $O_i^{\mathrm{Al}}(t)$ have comparable values while the oxygen atom is moving across the interface. For $t > 0.45$ ps, $O_i^{\mathrm{Fe}}(t)$ becomes zero, while $O_i^{\mathrm{Al}}(t)$ converges to a finite value, indicating that the oxygen atom is chemically bonded only with Al atoms.

Figure 8 shows the time evolution of $O_i(t)$ and $O_i^{\alpha}(t)$ for some oxygen atoms, which are selected from the six layers in the initial hematite crystal as shown by arrows in the figure. Note that, while $O_i(t)$ and $O_i^{\alpha}(t)$ are displayed for only 0.8 ps in Fig. 7, they are shown for 10 ps in Fig. 8. The plot in Fig. 7 corresponds to Fig. 8(a). It is seen that most oxygen atoms

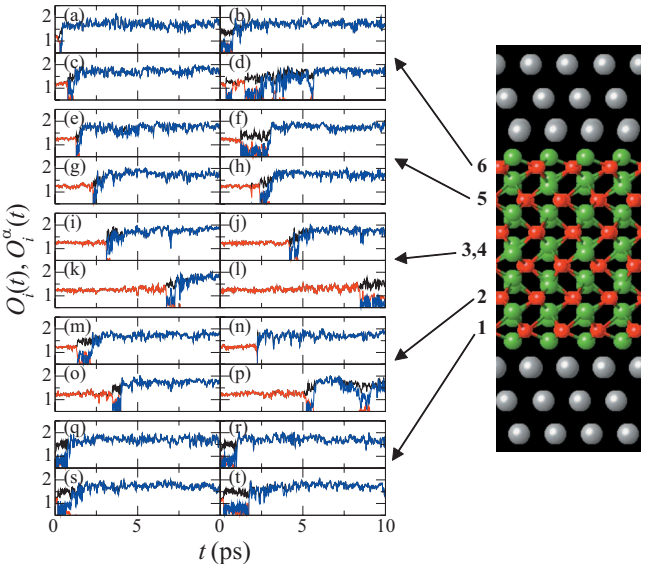

FIG. 8. (Color) Time evolution of the total and partial SBOP, $O_i(t)$ and $O_i^{\alpha}(t)$, associated with selected oxygen atoms. The black, red, and blue curves show $O_i(t)$, $O_i^{\mathrm{Fe}}(t)$, and $O_i^{\mathrm{Al}}(t)$, respectively. They are grouped according to the z positions in the initial atomic configuration as shown by arrows.

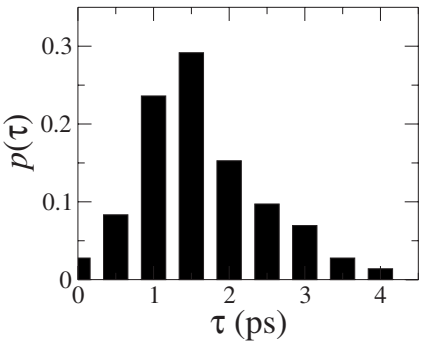

FIG. 9. Distribution $p(\tau)$ of the reaction time τ of oxygen atoms.

in the first and sixth layers form aluminum oxide within 2 ps as shown in Figs. 8(a)–8(c) and 8(q)–8(t). Figure 8(d) is for an oxygen atom that migrates to near Fe atoms entering the upper aluminum side, and $O_i^{\mathrm{Fe}}(t)$ has finite values up to about 6 ps. While almost all oxygen atoms in the fifth layer are bonded with Al atoms before 3 ps as shown in Figs. 8(e)–8(h), oxygen atoms in the second layer keep Fe-O bonds longer times, which exceed 5 ps in some cases as shown in Fig. 8(p). These correspond to the fact that the second oxygen layer is preserved up to 3 ps, while the fifth oxygen layer disappears before 3 ps as seen in Fig. 4. In the middle third and forth layers, oxygen atoms keep Fe-O bonds up to at least 3 ps and at longest 8 ps as shown in Figs. 8(i)–8(l).

F. Reaction time

As demonstrated in Figs. 7 and 8, the SBOP provides useful information about the bonding properties of each oxygen atom. To estimate the reaction time τ for each oxygen atom, we introduce a quantity $O_i^{\mathrm{Fe}}(t)/O_i(t)$, which is a measure of the chemical character of the ith oxygen atom; it is one for the oxygen atom in iron oxide, zero in the aluminum oxide, and ~ 0.5 at the interface. Using this quantity, we define the reaction time τ as the time taken for $O_i^{\mathrm{Fe}}(t)/O_i(t)$ to change from 0.9 to 0.1. For the oxygen atom in Fig. 7, for example, the estimated reaction time is $\tau \sim 0.25$ ps. The distribution $p(\tau)$ of the reaction time τ is shown in Fig. 9. $p(\tau)$ has a peak at about $\tau = 1.5$ ps, and distributes over 4 ps. The reaction time averaged over all oxygen atoms is $\langle \tau \rangle = 1.7 \pm 0.9$ ps, with the longest and shortest times being 4.2 and 0.14 ps, respectively.

G. Reaction rate

To quantify the rate of the thermite reaction, we calculate the average of $O_i^{\mathrm{Fe}}(t)/O_i(t)$ over all oxygen atoms

$$c_{\mathrm{Fe_2O_3}}(t) = \frac{1}{N_{\mathrm{O}}} \sum_{i \in \mathrm{O}} O_i^{\mathrm{Fe}}(t)/O_i(t), \tag{12}$$

where N_{O} is the number of oxygen atoms. $c_{\mathrm{Fe_2O_3}}(t)$, the ratio of the number of Fe-O chemical bonds to the number of all chemical bonds associated with oxygen atoms, is proportional to the amount of iron oxide. At the beginning of the

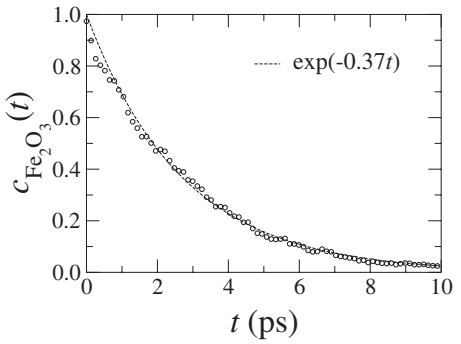

FIG. 10. Time evolution of the concentration of iron oxide in the thermite reaction $c_{Fe_2O_3}(t)=O_i^{Fe}(t)/[O_i^{Fe}(t)+O_i^{Al}(t)]$. The dashed curve shows the least-square fit $c_{Fe_2O_3}(t)=\exp(-0.37t)$.

simulation, all oxygen atoms reside in iron oxide and $c_{Fe_2O_3}(t)$ is unity; $c_{Fe_2O_3}(t)$ becomes zero after the redox reaction is completed. Figure 10 shows the time evolution of $c_{Fe_2O_3}(t)$. It is seen that $c_{Fe_2O_3}(t)$ decreases exponentially in the thermite reaction of a thin hematite layer with aluminum metal. The time constant for the exponential decay is estimated to be $1/0.37=2.7$ ps using the least-square fit.

IV. SUMMARY

In summary, we have investigated a thermite reaction of Fe_2O_3 with aluminum metal by molecular-dynamics simulations with interatomic forces calculated in the DFT framework. A redox reaction to form iron metal and Al_2O_3 has been found to initiate with the rapid formation of Al-O bonds at the interface within 1 ps, followed by the propagation of the combustion front with a velocity of 70 m/s for at least 5 ps at temperature 2000 K. The reaction time for an oxygen atom to change from the Fe_2O_3 to the Al_2O_3 character at the interface has been estimated to be 1.7 ± 0.9 ps, and bond-overlap population analysis has been used to calculate reaction rates. Such an atomistic description of the initial thermite reaction, especially at large length scales using multiscale QM-MD approaches [26,27] to describe realistic Al-nanoparticle–Fe_2O_3 structures (which involve multimillion atoms), is vital for understanding the fast reactions found in the nanothermite composites, which should be amenable to experimental measurements based on laser flash heating and picosecond spectroscopy [28].

The present *ab initio* MD study based on the explicit integration of Newton's equation of motion has shed light on initial thermite reactions. Longer-time dynamics issues (e.g., linear versus parabolic growth) may instead be studied with molecular-kinetics simulation based on the transition-state theory [29,30].

ACKNOWLEDGMENTS

This work was partially supported by ARO-MURI, DOE-BES, DOE-SciDAC, DTRA, and NSF-ITR. F.S. acknowledges support by Grant-in-Aid for Scientific Research on Priority Area, "Nanoionics (439)" from the MEXT, Japan. Simulations were performed at the University of Southern California using the 6020-processor Linux cluster at the Research Computing Facility and the 2048-processor Linux cluster at the Collaboratory for Advanced Computing and Simulations.

[1] L. L. Wang, Z. A. Munir, and Y. M. Maximov, J. Mater. Sci. **28**, 3693 (1993).
[2] R. A. Yetter, F. L. Dryer, M. T. Allen, J. L. Gatto, and J. Propul, Power **11**, 683 (1995).
[3] B. M. Rice, W. Mattson, J. Grosh, and S. F. Trevino, Phys. Rev. E **53**, 611 (1996).
[4] W. H. Wilson, M. P. Kramer, and R. W. Armstrong, Abstr. Pap. - Am. Chem. Soc. **221**, U608 (2001).
[5] M. M. Hurley, C. F. Chabalowski, G. H. Lushington *et al.*, Abstr. Pap. - Am. Chem. Soc. **220**, U284 (2000).
[6] K. L. McNesby, A. W. Miziolek, T. Nguyen *et al.*, Combust. Flame **142**, 413 (2005).
[7] K. I. Nomura, R. K. Kalia, A. Nakano, P. Vashishta, A. C. T. van Duin, and W. A. Goddard, Phys. Rev. Lett. **99**, 148303 (2007).
[8] K. B. Plantier, M. L. Pantoya, and A. E. Gash, Combust. Flame **140**, 299 (2005).
[9] B. S. Bockmon, M. L. Pantoya, S. F. Son, B. W. Asay, and J. T. Mang, J. Appl. Phys. **98**, 064903 (2005).
[10] V. I. Levitas, B. W. Asay, S. F. Son, and M. Pantoya, Appl. Phys. Lett. **89**, 071909 (2006).
[11] V. Tomar and M. Zhou, Appl. Phys. Lett. **88**, 233107 (2006).
[12] V. Tomar and M. Zhou, Phys. Rev. B **73**, 174116 (2006).
[13] J. P. Perdew, K. Burke, and M. Ernzerhof, Phys. Rev. Lett. **77**, 3865 (1996).
[14] G. Kresse and J. Hafner, Phys. Rev. B **49**, 14251 (1994).
[15] F. Shimojo, R. K. Kalia, A. Nakano, and P. Vashishta, Comput. Phys. Commun. **140**, 303 (2001).
[16] D. Vanderbilt, Phys. Rev. B **41**, 7892 (1990).
[17] S. Nosè, Mol. Phys. **52**, 255 (1984); W. G. Hoover, Phys. Rev. A **31**, 1695 (1985).
[18] M. Tuckerman, B. J. Berne, and G. J. Martyna, J. Chem. Phys. **97**, 1990 (1992).
[19] R. S. Mulliken, J. Chem. Phys. **23**, 1833 (1955); **23**, 1841 (1955).
[20] D. Sánchez-Portal, E. Artacho, and J. M. Soler, J. Phys.: Condens. Matter **8**, 3859 (1996).
[21] M. D. Segall, R. Shah, C. J. Pickard, and M. C. Payne, Phys. Rev. B **54**, 16317 (1996).
[22] F. Shimojo, K. Hoshino, and Y. Zempo, J. Phys. Soc. Jpn. **72**, 2822 (2003).
[23] P. E. Blöchl, Phys. Rev. B **50**, 17953 (1994).
[24] O. F. Sankey and D. J. Niklewski, Phys. Rev. B **40**, 3979 (1989).
[25] J. M. Soler, E. Artacho, J. D. Gale, A. García, J. Junquera, P. Ordejón, and D. Sánchez-Portal, J. Phys.: Condens. Matter **14**, 2745 (2002).

[26] J. Q. Broughton, F. F. Abraham, N. Bernstein, and E. Kaxiras, Phys. Rev. B **60**, 2391 (1999).
[27] S. Ogata, E. Lidorikis, F. Shimojo, A. Nakano, P. Vashishta, and R. K. Kalia, Comput. Phys. Commun. **138**, 143 (2001).
[28] Y. Q. Yang, S. F. Wang, Z. Y. Sun, and D. D. Dlott, Appl. Phys. Lett. **85**, 1493 (2004).
[29] A. Nakano, Comput. Phys. Commun. **176**, 292 (2007).
[30] A. Nakano, Comput. Phys. Commun. **178**, 280 (2008).